Field-induced transformation of complex spin ordering and magnetodielectric and magnetoelastic coupling in $MnGeTeO_6$

Y. H. Chang [1], Arkadeb Pal [1,2,3,*], P. T. W. Yen [1], C. W. Wang [4], S. Giri [2], G. R. Blake [3], Javier Gainza [5], M.-J. Hsieh [6], J.-Y. Lin [6,7], C. Y. Huang [1], Y. J. Chen [1], T. W. Kuo [1], Ajay Tiwari [1], D. Chandrasekhar Kakarla [1], and H. D. Yang [1,8,†]

[1] *Department of Physics, National Sun Yat-sen University, Kaohsiung 80424, Taiwan*
[2] *School of Physical Sciences, Indian Association for the Cultivation of Science, Kolkata 700032, India*
[3] *Zernike Institute for Advanced Materials, University of Groningen, 9700 AB Groningen, The Netherlands*
[4] *National Synchrotron Radiation Research Centre, Hsinchu 300092, Taiwan*
[5] *European Synchrotron Radiation Facility, 71 Avenue des Martyrs, 38043 Grenoble, France*
[6] *Institute of Physics, National Yang Ming Chiao Tung University, Hsinchu 300093, Taiwan*
[7] *Center for Emergent Functional Matter Science, National Yang Ming Chiao Tung University, Hsinchu 300093, Taiwan*
[8] *Center of Crystal Research, National Sun Yat-sen University, Kaohsiung 80424, Taiwan*

(Received 22 May 2024; accepted 17 July 2024; published 5 August 2024)

Spin-frustrated systems are well known for exhibiting fascinating and exotic magnetic properties and are often intertwined with other intriguing phenomena. Magnetization and specific-heat studies suggest that the spin-frustrated chiral triangular lattice compound $MnGeTeO_6$ undergoes a long-range antiferromagnetic transition below the Néel temperature (T_N) $\sim$ 9 K, which is further validated in the neutron powder-diffraction (NPD) study. In the absence of an external magnetic field (H), analysis of NPD data reveals a complex incommensurate spin structure, characterized by a mixture of helical and cycloidal spin orderings with a propagation vector of $\boldsymbol{k}$ = (1/3, 1/3, 0.184). Upon the application of H, this spin ordering transforms into a conical spin structure, which is manifested as a metamagnetic transition in the isothermal magnetization (M) curve when H exceeds $\sim$ 0.9 T. Total energy calculations and estimation of various exchange-interaction energies (J) by density-functional theory calculations also support the formation of such a complex spin ordering. Moreover, a pronounced dielectric (ε') anomaly is observed near T_N, which is suppressed considerably under H. The variation of ε' with increasing H closely reflects the $\Delta\varepsilon' \propto M^2$ scaling behavior in the low-H regime, thus indicating a higher-order magnetoelectric coupling. Moreover, synchrotron x-ray diffraction reveals an isostructural distortion below T_N, suggesting magnetoelastic coupling as a trigger for the dielectric anomaly.

DOI: 10.1103/PhysRevB.110.064405

I. INTRODUCTION

Geometrically frustrated magnets, which are distinguished by complex relationships among magnetic interactions and quantum spin fluctuations, have garnered widespread attention from the global scientific community. These materials exhibit numerous fascinating low-temperature phenomena arising from their diverse magnetic interactions. Notable examples include exotic quantum states such as spin liquids, spin ice, and magnetization plateaus [1–4]. Magnetic frustration arises primarily from the geometric arrangement of spins in certain lattice structures. This phenomenon is particularly prominent in systems with specific lattice configurations, such as two-dimensional (2D) triangular or kagome lattices, or three-dimensional (3D) pyrochlore or hyperkagome lattices. Triangular lattice antiferromagnets (TLAFs), as the simplest geometrically frustrated motif, have received considerable attention recently. In these systems, the nearest-neighbour spin interactions tend to be antiferromagnetic (AFM), which contributes to the complexity of their behavior. This frustration is typically manifested in a broad spectrum of exotic phenomena, including unconventional spin structures, field-induced magnetization plateaus, quantum spin liquids, and multiferroicity, which deviate from the traditional ferromagnetic or antiferromagnetic behaviors, thereby enriching the magnetic landscapes [5–14].

Furthermore, the increasing demand for advanced spintronic devices has propelled research into multifunctional materials that can respond to various external stimuli. These materials exhibit a diverse array of intriguing properties, which typically arise from the intricate interplay of microscopic order parameters, including spin, lattice, orbital, dipole, and phonon interactions [15–23]. In this context, considerable research effort has been dedicated to investigating novel multiferroic and magnetodielectric (MD) phenomena in such frustrated magnets [15,17,24], for which a comprehensive understanding of their spin structures is crucial. The MD effect across various classes of magnetic systems has been investigated extensively [21,22,25–29]. However, the scarcity of such materials persists due to the inherent antagonistic origins of their magnetic and ferroelectric properties. TLAFs are notable for their distinctive noncollinear chiral spin

*Contact author: pal.arkadeb@gmail.com
†Contact author: yang@mail.nsysu.edu.tw

ordering, which can result in the MD effect and/or spin-driven ferroelectricity.

In this context, the layered TLAF system, $MnGeTeO_6$ (MGTO), emerges as an intriguing candidate for investigating the properties outlined above. The synthesis, crystal structure, and bulk magnetization of this compound were first reported by Kim *et al.* in 2017 [30]. When considering both nonmagnetic ions Ge^{4+} and Te^{6+} ions, the structure of MGTO reveals a layered honeycomb lattice on the *ab* plane. However, a triangular layer of magnetic Mn ions is present between the two honeycomb layers, thus rendering the present system a layered TLAF system. Furthermore, its crystalline structure belongs to a noncentrosymmetric (NCS) trigonal system with space group *P*312. The coexistence of a spin-frustrated triangular lattice with an NCS polar crystal structure often triggers the emergence of complex noncollinear and noncoplanar spin structures, alongside intriguing magnetoelectric (ME) properties. These facts motivated us to conduct a comprehensive study aimed at exploring the intriguing spin ordering and its implications on the crystal structure and dielectric properties of MGTO.

II. EXPERIMENTAL AND COMPUTATIONAL METHODS

Polycrystalline MGTO samples were synthesized via the standard solid-state reaction method. High-purity oxide powders (>99.99%, Alfa-Aesar) of $MnCO_3$, H_6TeO_6, and GeO_2 were used as precursors. The preparation involved a two-step process. First, $MnGeO_3$ was synthesized by heating a thoroughly ground mixture of $MnCO_3$ and GeO_2 (at an appropriate stoichiometric ratio) at 1150 °C for 18 h in air. The prepared $MnGeO_3$ was mixed with H_6TeO_6, and the resulting powder was pressed into a pellet, which was then subjected to heating at 700 °C for 30 h under O_2 flow with one intermediate regrinding. The phase purity of the final product was confirmed using a room-temperature high-resolution synchrotron x-ray-diffraction (SXRD) measurement, which was conducted at the Taiwan Photon Source 19A beamline of the National Synchrotron Radiation Research Center, Taiwan, utilizing x rays with a wavelength of 0.619 92 Å. Additionally, temperature (*T*)-dependent high-resolution synchrotron SXRD patterns were acquired over the range of 200 to 4 K at the ID22 beamline, situated at the European Synchrotron Radiation Facility (ESRF) in Grenoble, France, wherein the x-ray beam utilized had a wavelength of 0.426 22 Å. Bulk magnetization studies were performed using a superconducting quantum interference device (SQUID)-based magnetic property measurement system (Quantum Design). *T*-dependent specific-heat (C_P) measurements were conducted via a heat-pulsed thermal relaxation calorimeter in a physical property measurement system. *T*- and *H*-dependent dielectric measurements were performed using an Agilent precision E4980A LCR meter attached to the commercial SQUID-based magnetometer, where a custom-developed dielectric probe was utilized. NPD measurements were conducted at the Australian Nuclear Science and Technology Organization in Sydney, using a high-intensity neutron-powder diffractometer known as WOMBAT and a high-resolution neutron-powder diffractometer named ECHIDNA employing neutrons with a wavelength (λ) of 4.63 and 2.4395 Å, respectively [31,32]. The NPD data were analyzed using the FULLPROF SUITE package software. The lattice parameters and atomic coordinates were extracted from the Rietveld refinement of the SXRD data, as shown in the Supplemental Material (SM) [33].

Density-functional theory (DFT)-based *ab initio* calculations have been performed using VASP version 6.1.2. The experimentally obtained lattice parameters were used for the initial input. The basis sets selected for Mn, Ge, Te, and O are the projector-augmented plane-wave method, and a plane-wave cutoff value was set to 400 eV. The exchange-correlation functional used was GGA-PBE (generalized gradient approximation-Perdew-Burke-Ernzerhof). We relaxed the cell shape, volume, and its atomic positions while preserving its space-group symmetry *P*312. To include the electron correlation interaction in this material, we used a Hubbard *U* value of 3.9 eV on the Mn site [34]. Furthermore, spin-spiral calculations were conducted by relaxing the spin structure to estimate the magnetic ground state using VASP, version 6.1.2. Utilizing the generalized Bloch condition, we could avoid the requirement of a large supercell to simulate spin interactions, even in the presence of a spin spiral arising from an incommensurate wave. Moreover, various exchange-interaction energies (*J*) were calculated by using a Heisenberg model constructed via the TB2J approach. The numerical approach to fit the exchange parameters is described in SM [33] (see also Refs. [35,36] therein).

III. RESULTS AND DISCUSSION

A. Crystal structure

The high-resolution SXRD pattern of MGTO recorded at $T = 300$ K and its calculated profile (obtained via Rietveld refinement) are shown in Fig. 1(a). Structural analysis yielded a single-phase trigonal crystal structure with an NCS *P*312 space group. No traces of impurity phases were detected. The obtained lattice parameters, Wyckoff positions, and related data are summarized in SM [33], and show good agreement with previously reported values. A schematic representation of the crystal structure (viewed on the *ab* plane) obtained from the SXRD data analysis is illustrated in Fig. 1(b). The structure comprises an interconnected network of MnO_6, GeO_6, and TeO_6 octahedra. Here, the Mn^{2+} ions form a 2D layered triangular lattice on the *ab* plane, whereas the GeO_6 and TeO_6 octahedra form a 2D honeycomb lattice between two successive layers of the triangular Mn lattice.

B. Magnetization (*M*) properties

M as a function of *T* under $H = 0.1$ T was recorded using the standard zero-field cooling (ZFC) and field-cooling (FC) methods, as shown in Fig. 2(a). A long-range ordered (LRO) AFM state emerged at $T_N \sim 9$ K, evidenced by a cusp in the *M* (*T*) curves, which is a typical feature of AFM ordering. Moreover, ZFC and FC *M* (*T*) curves measured under $H = 1$ T are demonstrated in the inset of Fig. 2(a). A clear magnetic transition is also evident from these curves at $T_N \sim 9$ K. However, the nature of the curves has changed in this case by showing an increasing trend in *M* below $T_N \sim 9$ K, which may be presumably attributed to an altered spin structure (this will be discussed in the following section). The

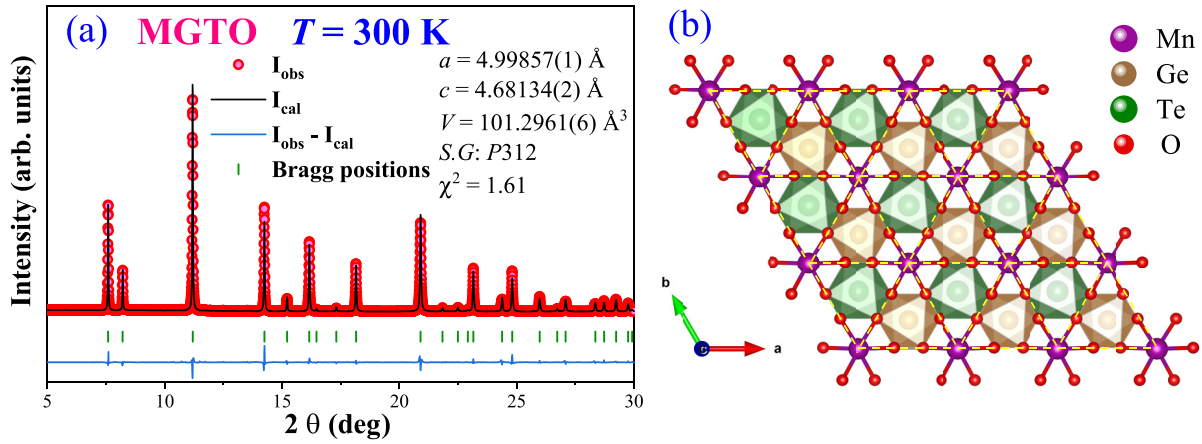

FIG. 1. (a) SXRD pattern at $T = 300$ K along with its Rietveld refinement. The red circles represent the data, while the black solid line refers to the calculated Rietveld profile. The green vertical bars refer to the Bragg positions. (b) The polyhedral representation of the crystal structure of MGTO as projected on the *ab* plane. Purple, brown, green, and red spheres stand for Mn, Ge, Te, and O atoms, respectively. The yellow dashed lines act as a guide to the eye, and demonstrate a triangular lattice formed by the magnetic ions Mn^{2+}.

standard Curie-Weiss (CW) fitting was performed on the "inverse susceptibility $(1/\chi)$ vs T" data (recorded under $H = 1$ T) in the considerably elevated T range ($T > 100$ K). The CW law is expressed as $\chi = \chi_0 + \frac{C}{T-\theta_{CW}}$, where C refers to the Curie constant; χ_0 represents the T-independent susceptibility which comprises two different parameters, including the core diamagnetism appearing due to the core-electron shells (χ_{core}) of the Mn^{2+} ions of MGTO and the Van Vleck paramagnetism

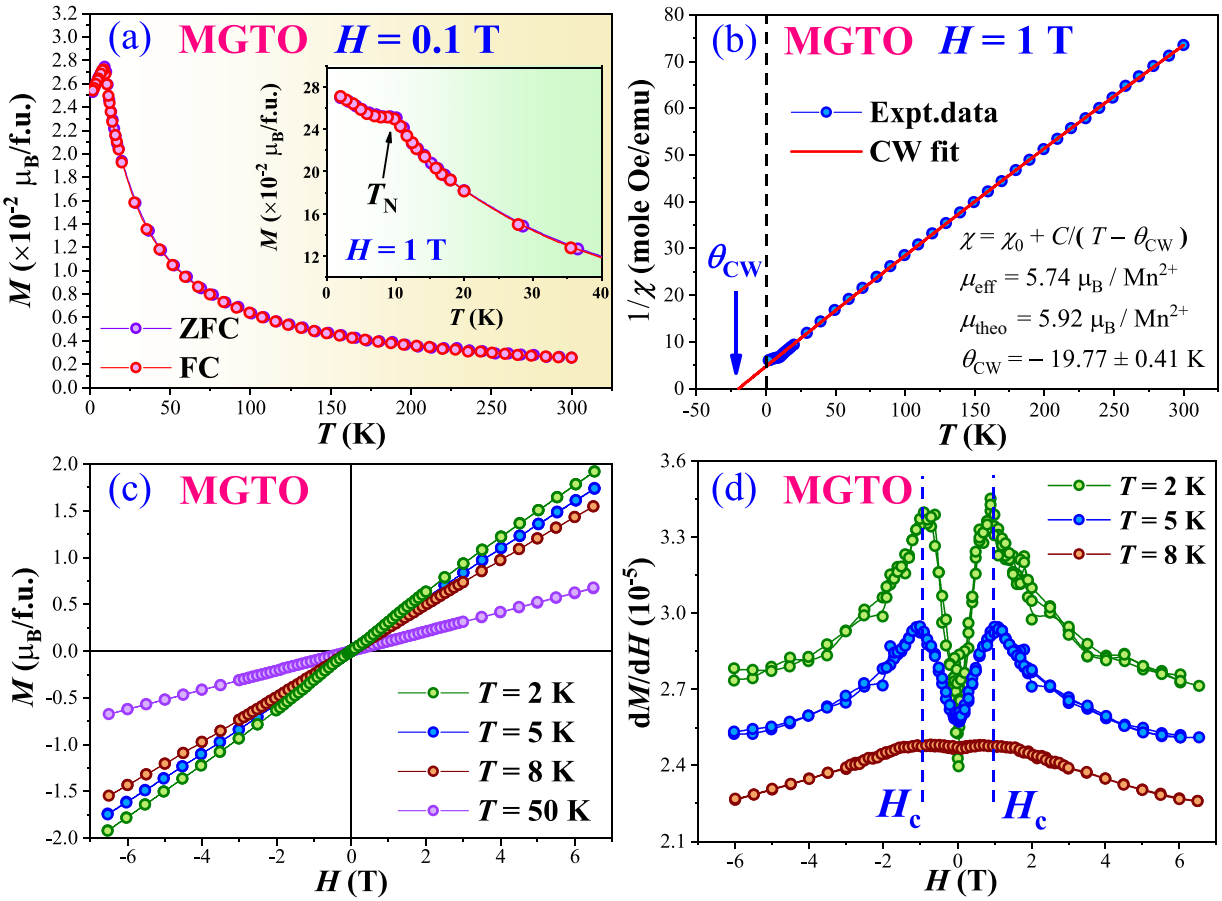

FIG. 2. (a) Temperature variations of the ZFC and FC magnetization curves recorded under $H = 0.1$ T. Inset: M (T) curves collected at $H = 1$ T. (b) Inverse dc susceptibility $(1/\chi)$ curve (at $H = 1$ T) with varying temperature and its corresponding Curie-Weiss fit (red line) performed in the paramagnetic region. (c) The magnetic field variation of the isothermal magnetization curves recorded at various temperatures. (d) The *dM/dH* curves as a function of *H,* at $T = 2$, 5, and 8 K. The metamagnetic transition is visible near a critical field of H_c.

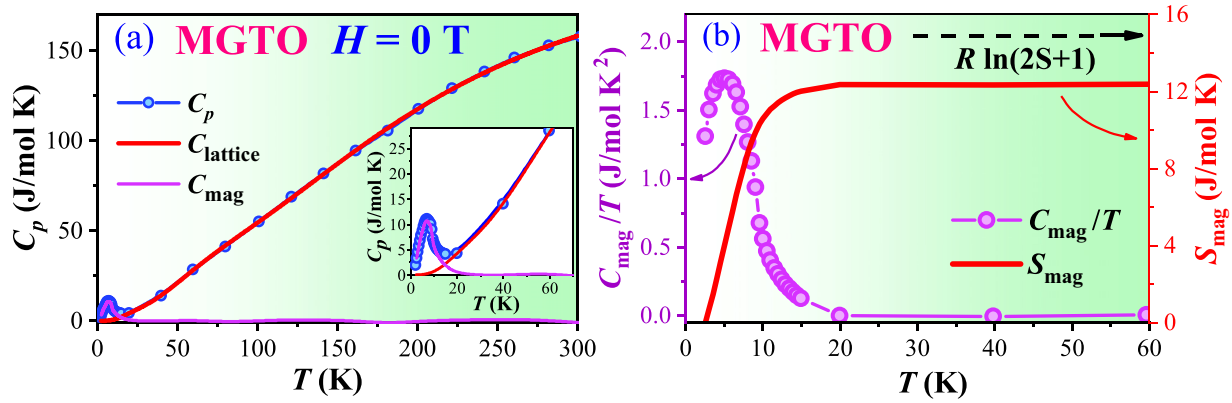

FIG. 3. (a) Specific-heat curve measured under zero magnetic field. The red and purple lines represent the phononic (C_{lattice}) and magnetic (C_{mag}) parts of C_P (T), respectively. Inset: A close view of (a) around T_{N}. (b) C_{mag}/T curve as a function of temperature and its corresponding magnetic entropy S_{mag} curve. The dashed arrow points to the expected value of magnetic entropy $S_{\text{mag}} = R\ln(2S+1) \sim 14.9\,\text{J/mol K}$ for $Mn^{2+}(S = 5/2)$.

(χ_{VV}) owing to its open-shell electrons; and θ_{CW} indicates the characteristic CW temperature. Figure 2(b) shows the best fitting, which yielded $\chi_0 = 7.4 \times 10^{-4}$ emu/(mole Oe); the effective paramagnetic moment, i.e., $\mu_{\text{eff}} = 5.74\ \mu_{\text{B}}/Mn^{2+}$; and $\theta_{\text{CW}} = -19.77$ K. The negative value of θ_{CW} indicates the presence of dominant AFM interactions among Mn^{2+} spins. Moreover, the experimentally obtained $\mu_{\text{eff}} = 5.74\ \mu_{\text{B}}/Mn^{2+}$ showed a close match with the calculated spin-only moment of Mn^{2+} ions, i.e., $\mu_{\text{theo}} = 5.92\ \mu_{\text{B}}/Mn^{2+}$.

The isothermal M curves recorded with varying H, i.e., M (H) curves at various T values such as $T = 2$, 5, 8, and 50 K for MGTO, are shown in Fig. 2(c). Below T_{N}, the M (H) curves exhibited an almost linear behavior without any sizable hysteresis for the entire investigated range of H. No sign of M saturation was observed, even at $H = 7$ T. However, a small but discernible slope change which led to a slight nonlinearity in the M (H) curves was observed as H increased beyond $\sim$ 0.9 T. This is more evident in the corresponding dM/dH curves, which showed pronounced anomalies near the critical field $H_{\text{c}} = 0.9$ T, as shown in Fig. 2(d). This metamagnetic transition is attributable to a field-induced spin-flop transition. In fact, a field-induced spin structure change was indeed observed from our NPD study, which will be discussed in the following section. Moreover, the M (H) curve recorded at $T = 50$ K is nonsaturating and completely linear, which is a typical characteristic of the paramagnetic state of the antiferromagnets, thus corroborating the M (T) data.

C. Specific-heat properties

Specific-heat (C_P) measurements were performed to further investigate the nature of magnetic ordering in MGTO. The C_P (T) data measured at $H = 0$ T are shown in Fig. 3(a), which exhibit a clear anomaly at $T_{\text{N}} \sim 9$ K, thus confirming the onset of an LRO AFM state below 9 K. This supports the results of the bulk M study and the microscopic spin structure measurements conducted via NPD studies of this system (related discussions regarding the investigation of the spin structure are provided in the following section). In insulating magnetic systems, C_P (T) arises from two distinct sources: the phononic contribution at high T and the magnetic contribution at considerably lower T. To determine the magnetic specific heat (C_{mag}), we isolated the phononic contribution (C_{lattice}) by subtracting it from the total C_P. C_{lattice} was obtained by fitting our C_P (T) data in the high-T range (30−300 K) and subsequently extrapolating it down to 2 K [as illustrated by the red line in Fig. 3(a)] using the Debye-Einstein model, as expressed below [37]:

$$\begin{aligned} C_{\text{lattice}} &= C_{\text{Debye}}(T) + C_{\text{Einstein}}(T) \\ &= n_{\text{D}}\left[9R\left(\frac{T}{\theta_{\text{D}}}\right)^3 \int_0^{\theta_{\text{D}}/T} \frac{x^4 e^x}{(e^x-1)^2} dx\right] \\ &\quad + \sum_{\text{i}} 3n_{\text{Ei}}\text{R}\left(\frac{\theta_{E_i}}{T}\right)^2 \frac{e^{\theta_{E_i}/T}}{(e^{\theta_{E_i}/T}-1)^2}. \end{aligned} \tag{1}$$

Here, the first term denotes acoustic phonons (as described by the Debye model), the second term refers to optical phonons (following the Einstein model), and n_{D} and n_{Ei} denote their respective weighting factors. In this case, $n_{\text{D}} + \sum_{\text{i}} n_{\text{Ei}} = n = 9$ indicates the total number of atoms per formula unit of MGTO. Meanwhile, θ_{D} and θ_{Ei} refer to the Debye and Einstein temperatures, respectively. The best fit for the measured C_P (T) data of MGTO using the aforementioned model yielded a single Debye branch ($n_{\text{D}} = 1$, $\theta_{\text{D}} = 118$ K) and two Einstein branches (($n_{E1} = 3$, $\theta_{E1} = 257$ K, $n_{E2} = 5$, $\theta_{E2} = 735$ K). The T dependence of the C_{mag}/T curve after subtracting C_{lattice} is shown in Fig. 3(b). This curve was further integrated to obtain the magnetic entropy (S_{mag}), as shown in Fig. 3(b). However, only approximately 83% of the total S_{mag} was released at T_{N} and the remainder was restored above T_{N}. Additionally, S_{mag} attains a saturation value of $\sim$12.3 J/mol K, which was lower than the calculated total magnetic entropy expected for Mn^{2+} spins ($S = 5/2$) $\sim$14.9 J/mol K. It should be noted that the integration of the C_{mag}/T curve was performed starting from $T = 2$ K. Consequently, the lower temperature S_{mag} (below 2 K) was not included in the calculation, which would likely result in a slight underestimation of the saturation value of S_{mag}. Moreover, in the high-temperature regime, the overestimation of C_{lattice} might plausibly account for the significantly suppressed S_{mag} sat-

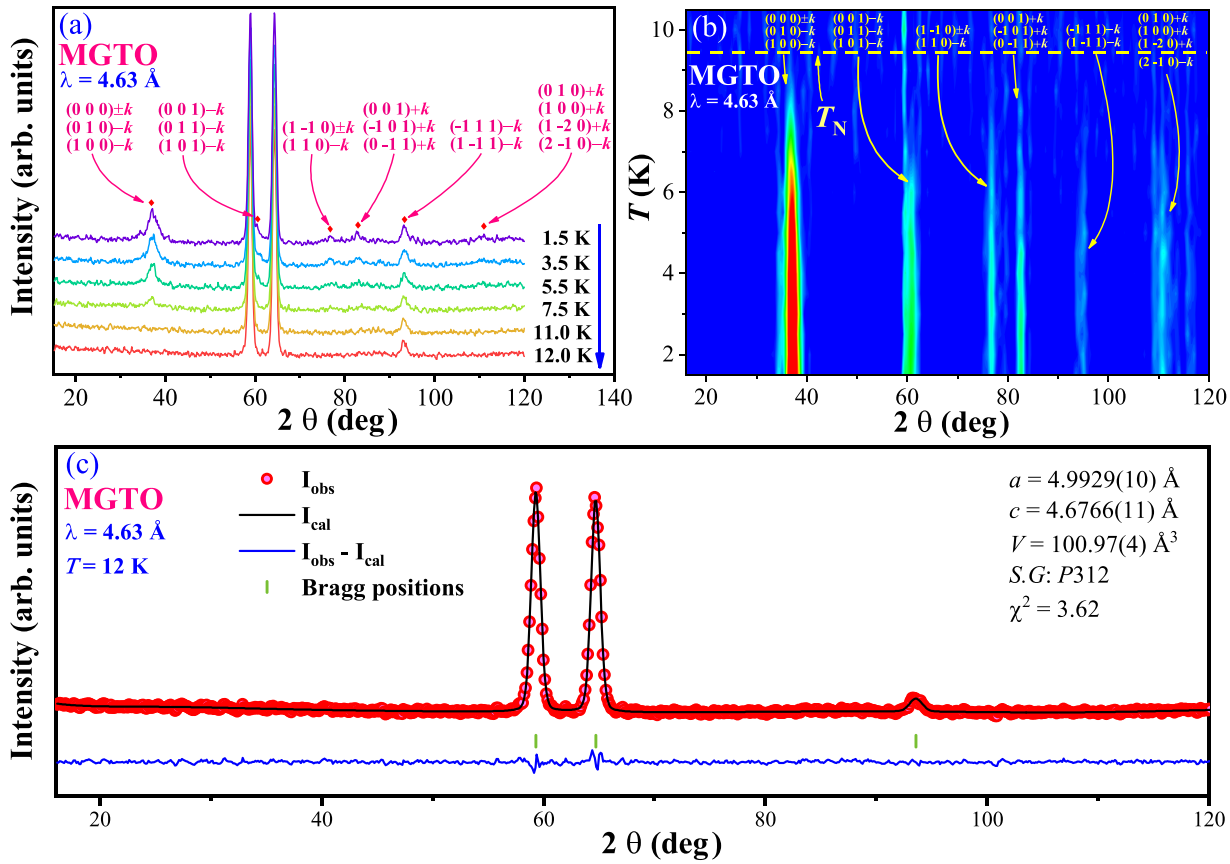

FIG. 4. (a) The measured NPD data (raw) at various temperatures. (b) The color-coded contour plot representing the relative intensity of NPD data, i.e., $I(T) - I$ (11 K) as a function of T and 2 θ. This demonstrates the emergence of various magnetic reflections below T_N. (c) The observed (red circles) NPD pattern at 12 K (above T_N) under $H = 0$ T and its corresponding best fit considering only a nuclear structure (i.e., structural symmetry $P312$).

uration value (approximately 83%). The missing magnetic entropy that remained underestimated above the LRO state may be attributable to the short-range magnetic ordering above T_N arising from the spin-frustrated low-dimensional nature of the present system. In fact, the observation of such reduced entropy has been reported in various other frustrated TLAF systems [37].

D. Neutron-powder diffraction: An incommensurate spin ordering

NPD patterns were recorded at various T, encompassing those both below and above the T_N of MGTO, to reveal the previously unknown microscopic spin structure of MGTO. The measured NPD data for some selected T values are shown in Fig. 4(a). Upon cooling to below T_N, another set of incommensurate magnetic (ICM) peaks appeared in the NPD patterns. These peaks could not be indexed to the fundamental unit cell, thus indicating an ICM-modulated spin structure. The most prominent magnetic Bragg reflection manifests at a lower diffraction angle, lying even below the appearance of the first nuclear reflection (0 0 1), strongly suggesting AFM ordering in the system. To identify the magnetic Bragg peaks appearing below T_N, the nuclear contribution (based on the data obtained at $T = 11$ K as reference) was subtracted from all the NPD data recorded at various T. The evolution of magnetic Bragg reflections with decreasing T below T_N became more evident through examination of the color-coded contour plot representing the relative intensity of NPD data $I(T) - I$ (11 K) as a function of T and 2 θ, as demonstrated in Fig. 4(b). Therefore, the NPD data above T_N were fitted satisfactorily, where the nuclear structure with trigonal symmetry was considered exclusively, as shown in Fig. 4(c). Meanwhile, the obtained NPD pattern containing the magnetic Bragg reflections at $T = 1.5$ K is shown in Fig. 5(a). Compared with the nuclear structural peaks at the base T of 1.5 K, the magnetic peaks display significant broadening, which is attributable to the finite magnetic correlation length within the ordered state. The data were fitted to several candidate ICM models, including the amplitude-modulated and orientation-modulated spin structures, as summarized in Table SII in SM [33]. The best fit yielded an ICM spin ordering represented by a propagation vector $\boldsymbol{k} = (1/3, 1/3, 0.184)$, which effectively indexed all the peak positions of the observed magnetic reflections, as demonstrated in Fig. 5(a). The spin structure obtained is shown in Fig. 5(b). The nature of the spin structure can be understood more clearly from Fig. 5(c), which depicts the spins propagating along the direction of $\boldsymbol{k}$ at a certain region presented in Fig. 5(b). The analysis suggests that the axis of the plane formed by the modulating spins and the propagation vector $\boldsymbol{k}$ has an angle of $\sim 10°$ between them, thus indicating a mixture of a cycloidal and a

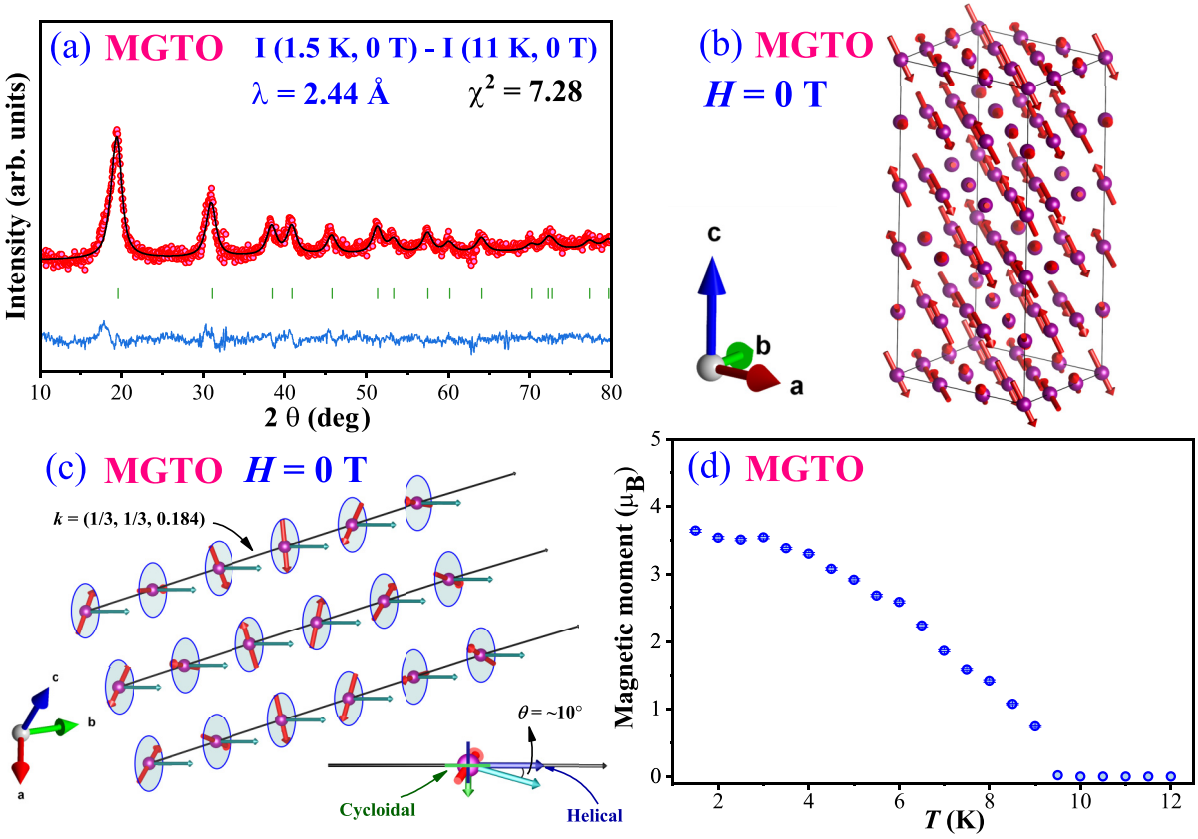

FIG. 5. (a) The observed (red circles) magnetic NPD pattern at 1.5 K recorded under $H = 0$ T, i.e., I (1.5 K, 0 T) − I (11 K, 0 T) and its corresponding best fit (black solid line) with $\boldsymbol{k} = (1/3, 1/3, 0.184)$. (b) A schematic representation of the spin structure obtained from the NPD fitting results. (c) The closer view of a certain part of the spin structure along with the direction of $\boldsymbol{k} = (1/3, 1/3, 0.184)$, where the Nile blue arrows represent the axis of the plane formed by spins. The inset depicts the components of cycloidal and helical spin structures. (d) T dependence of the magnetic moment.

helical spin structure in MGTO. In this case, the spin structure is predominantly helical, accounting for approximately 97%, while the cycloidal nature is minor, comprising around 3%. This signifies the incommensurability of the magnetic unit cell relative to the crystallographic unit cell in this system. Nevertheless, the obtained spin structure is closer to a helical ordering, whereas its cycloidal character is much weaker. The variation in the derived magnetic moment (m) as a function of T is shown in Fig. 5(d). The refined magnetic moment per Mn^{2+} ion at $T = 1.5$ K was approximately 3.6(1) μ_B/Mn^{2+}, which was considerably lower than the theoretically anticipated fully saturated moment of 5 μ_B ($S = 5/2$) for Mn^{2+} ions. This reduction in the moment can be plausibly ascribed to the effect of robust quantum fluctuations stemming from the low-dimensional nature of the system under investigation [38,39]. These fluctuations prevented the spins from achieving a fully ordered state.

A metamagnetic transition induced by H was observed in the M (H) study, which prompted further investigation via NPD measurements under a nonzero H to elucidate the potential changes in the spin structure. A field up to $H = 10$ T was applied in this study. Owing to the application of H, the NPD pattern was changed significantly, as illustrated in Fig. 6(a), which shows the comparison between NPD patterns recorded under $H = 0$ T and 10 T at $T = 1.5$ K. This unequivocally indicates a modified spin structure under the influence of H. Upon the application of H, the initially observed incommensurate peaks (at $H = 0$ T) sharpened, and a completely different set of commensurate magnetic peaks described by propagation vector $\boldsymbol{k} = (0, 0, 0)$ emerged in the NPD pattern. The coexistence of the fundamental $\boldsymbol{k} = (0, 0, 0)$ and an incommensurate modulation typically refers to either the coexistence of an incommensurate structure and a ferromagnetic (FM) phase or a conical spin structure, which cannot be distinguished with the Rietveld analysis. The positions of the incommensurate magnetic peaks remained unaltered, thus indicating that the magnetic periodicity was unaffected by the applied H up to 10 T. The best fitting of the NPD data at $H = 10$ T was obtained using a conical model [40]. The cone axis was first determined by refining an FM model with $\boldsymbol{k} = (0, 0, 0)$ against the fundamental peaks. The in-plane ferromagnetic component could not be determined by powder diffraction and was fixed to along the [1 1 0] direction. Furthermore, the analysis yielded a half-cone angle of $\alpha = 33.6°$. It can be noted that the cone axis points approximately 10 ° away from the propagation vector $\boldsymbol{k} = (1/3, 1/3, 0.184)$, which is consistent with the case of $H = 0$ T. The best fit to the NPD data for $H = 10$ T is shown in Fig. 6(b). The corresponding spin structure obtained from this analysis is shown in Fig. 6(c). A certain part of Fig. 6(c) is shown

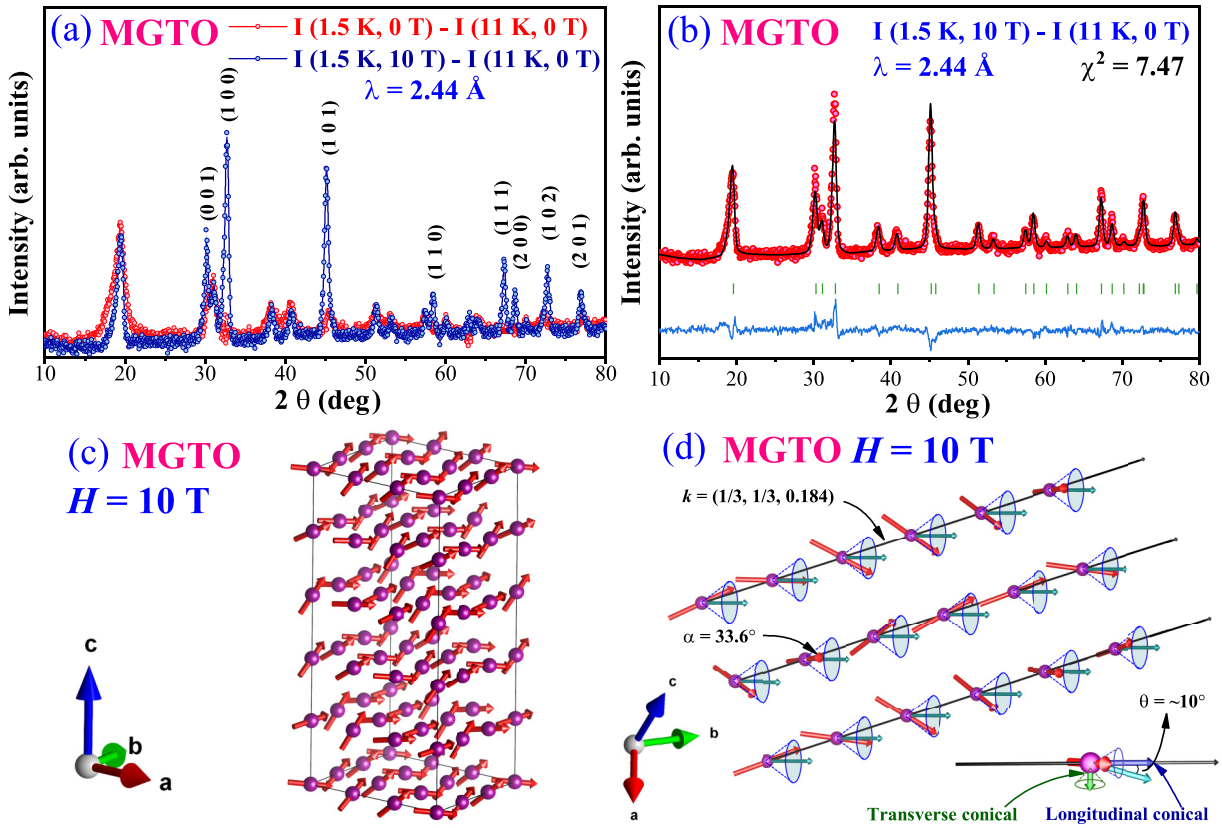

FIG. 6. (a) The experimentally observed magnetic Bragg peaks i.e., I (1.5 K, 0 T) − I (11 K, 0 T) and I (1.5 K, 10 T) − I (11 K, 0 T). (b) The observed (red circles) magnetic NPD pattern at 1.5 K recorded under $H = 10$ T, i.e., I (1.5 K, 10 T) − I (11 K, 0 T) and its corresponding best fit (black solid line) using the proposed conical model. (c) A pictorial illustration of the conical spin structure as obtained from the NPD data analysis. (d) The closer view of a certain part of the spin structure along with the direction of $\boldsymbol{k}$ =(1/3, 1/3, 0.184), where the Nile blue arrows represent the cone's axis. The inset depicts the components of a transverse and longitudinal conical spin structure.

in Fig. 6(d), which demonstrates a clear representation of the conical spin structure showing spin modulation along $\boldsymbol{k} = (1/3, 1/3, 0.184)$. Furthermore, the obtained conical spin structure can be described as a mixture of longitudinal and transverse conical spin ordering due to the presence of a 10° angle between the cone axis and $\boldsymbol{k}$. At $H = 10$ T, the value of the refined ordered magnetic moment is 4.28(2) μ_B/f.u. (where f.u. is formula units), which corresponds to a net magnetization of 3.56(2) μ_B/f.u. for this spin ordering. This is close to the extrapolated value of $M \sim 3$ μ_B/f.u. at $H = 10$ T from the M (H) curve recorded at $T = 2$ K. Hence, a field-induced transformation from a mixture of cycloidal and helical spin ordering to a conical spin ordering is inferred. Eventually, this transformation of spin order was also reflected in the variations of M and dielectric constant (ε') curves (will be discussed later) as the applied H increased beyond $H_c \sim 0.9$ T. Moreover, an altered conical spin structure may be hinted at by the modified pattern of the M (T) curves at $H = 1$ T, which showed an increasing trend in M [as shown in the inset of Fig. 2(a)].

E. Estimation of magnetic ground state by density-functional theory calculations

Furthermore, *ab initio* theoretical calculations have been performed on MGTO to get more insight into the magnetic ground state of this system. The total energies of the system with a similar spin structure (i.e., a combination of helical and cycloidal spin ordering) as observed by the NPD study at $H = 0$ T and a conical spin structure have been calculated by using the experimentally obtained $\boldsymbol{k}$ vector (1/3, 1/3, 0.184). The original conventional cell was expanded to a $3 \times 3 \times 5$ supercell. The simulated helical-cycloidal and conical spin structures are depicted in Figs. 7(a) and 7(b), respectively. For the estimation of the converged total energies, the following Hamiltonian based on a DFT framework was used, as expressed below:

$$\hat{H}_{DFT} = \hat{T}[n(r)] + E_{xc}[n(r)] + \frac{e^2}{2}\iint \frac{n(r)n(r')}{|r-r'|}drdr' + V_{ext}[n(r)], \quad (2)$$

where $n(r)$ is the ground-state electronic density, r the spatial coordinates, $\hat{T}$ the kinetic energy of electrons, E_{xc} the exchange-correlation potential, the third term refers to the Hartree potential, and V_{ext} is the external potential that describes the interaction of electrons and ions. The calculations revealed that the total energy obtained for the helical-cycloidal spin ordering ($E = -2553.443$ eV) was comparatively lower than that of the conical spin ordering ($E = -2552.751$ eV), indicating its preference as the energetically favorable ground

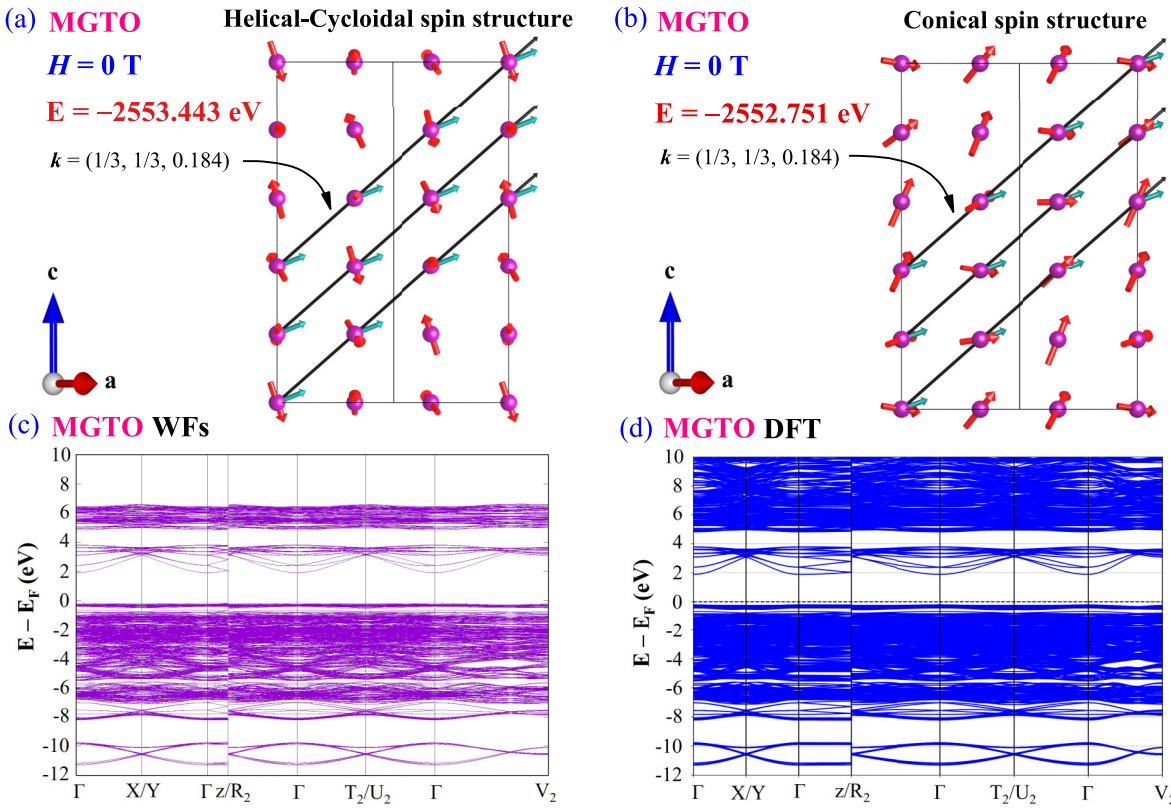

FIG. 7. The calculated total energies of magnetic states based on a DFT framework with $\boldsymbol{k} = (1/3, 1/3, 0.184)$ in different DFT-relaxed spin configurations of (a) the mixture of helical and cycloidal spin structure, and (b) the conical spin structure, respectively. The visual comparison of (c) the band structure of MGTO obtained from WFs and (d) the band structure obtained from DFT.

state for this system at $H = 0\,\mathrm{T}$. Thus, this corroborates the NPD results.

A complex noncollinear spin ordering in an NCS system usually emerges due to various competing magnetic exchange interactions (J) along with the Dzyaloshinskii-Moriya interaction (D). Therefore, to better understand the origin of the complex spin order in MGTO, we estimated various interactions occurring in MGTO. The magnetic interactions within a complex magnetic system can be summarized by the following general formula:

$$\hat{\mathrm{H}} = -\sum_{\mathrm{i}} \mathrm{K_i} \overrightarrow{S_i}^2 - \sum_{\mathrm{i}\neq j} \left[J_{\mathrm{ij}}^{\mathrm{iso}} \overrightarrow{s_i} \cdot \overrightarrow{s_j} + \overrightarrow{s_i}\, J_{\mathrm{ij}}^{\mathrm{ani}} \overrightarrow{s_j} + \overrightarrow{D_{ij}} \cdot (\overrightarrow{s_i} \times \overrightarrow{s_j}) \right],$$

where $\hat{H}$ refers to the Heisenberg Hamiltonian. The first term is associated with the single-ion anisotropy, J^{iso} represents isotropic exchange parameter, J^{ani} denotes the Kitaev-type exchange coupling or anisotropic exchange parameter, and $\overrightarrow{D_{ij}}$ corresponds to the Dzyaloshinskii-Moriya interaction (DMI) parameter. The DFT plane-wave results (for the helical-cycloidal spin structure) were transformed into the Wannier functions (WFs), which were then used in TB2J for estimating various exchange-interaction terms J^{iso}, J^{ani}, and D_{ij} for MGTO. The corresponding WFs-interpolated band structure is shown in Fig. 7(c). This closely matches with the band structure obtained by DFT calculations as depicted in Fig. 7(d), thus validating the WFs results. The exchange parameters thus obtained are demonstrated as a function of distance between two Mn spins in Fig. 8(a). Depending on the distances among spins, three main types of exchange interactions, denoted as J_1, J_2, and J_3, can be found in Fig. 8(a), which correspond to various Mn-Mn pair distances ~4.67, 4.99, and 6.84 Å, respectively, as illustrated in Figs. 8(b)–8(d). For all these magnetic exchange interactions, irrespective of the different Mn-Mn distances, the exchange pathways between Mn spins are always provided via TeO_6 or GeO_6 octahedra [as described in Figs. 8(b)–8(d)]. The strength and the nature of these exchange interactions are strongly influenced by the various exchange pathways involving different bond angles and bond lengths, which are governed by the Goodenough-Kanamori-Anderson rule. Even for a given Mn-Mn distance, there are numerous exchange pathways Mn-O-Ge-O-Mn and Mn-O-Te-O-Mn between two Mn spins, thus giving rise to different values of J. It is evident from Fig. 8(a) that J^{iso} is dominant for the J_3-type exchange interactions, which are mainly AFM in nature (carrying negative sign), except one point with small positive value indicating a weak ferromagnetic (FM) interaction. On the contrary, J^{iso} interactions for the Mn-Mn pairs with smaller distances (i.e., for J_1- or J_2 types) are relatively weak and FM in nature (with positive values). This suggests leading towards the presence of competing AFM (predominant) and FM interactions in

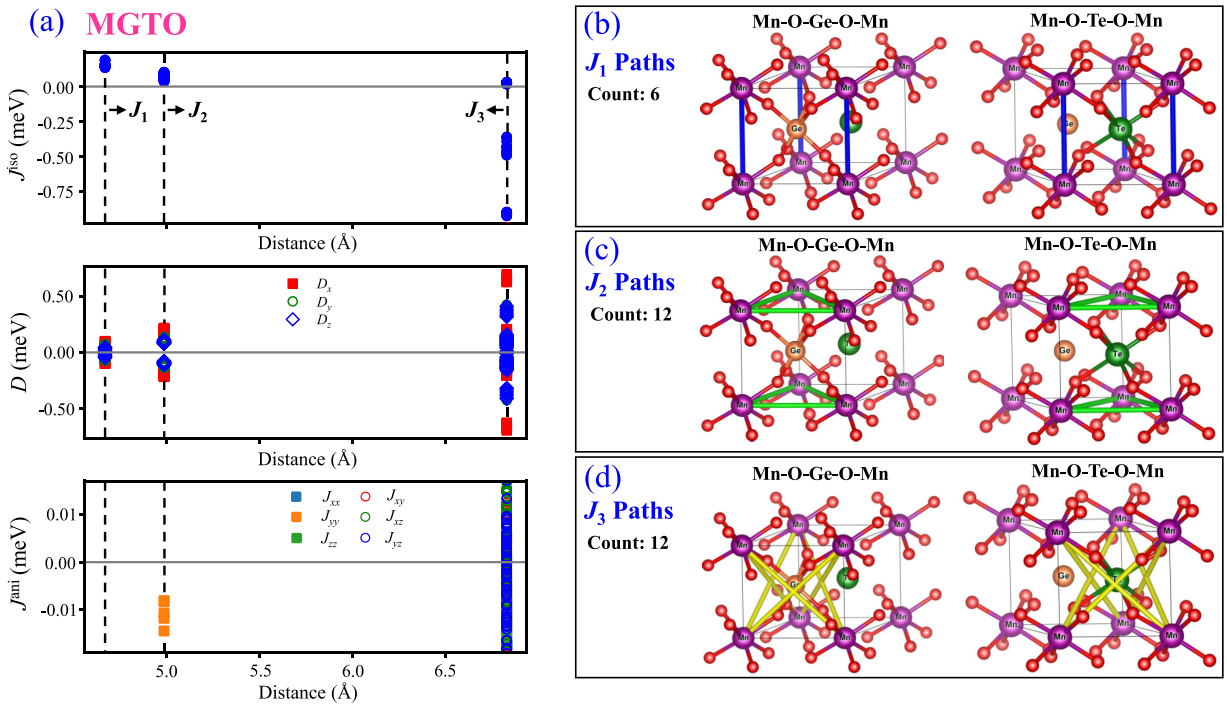

FIG. 8. (a) The J^{iso}, D, and J^{ani} calculated from TB2J for $MnGeTeO_6$. Here, J_1, J_2, and J_3 are denoted by black dashed lines, which correspond to various Mn-Mn pair distances of approximately 4.67, 4.99, and 6.84 Å, respectively. The graphical illustration of the paths of (a) J_1, (b) J_2, and (c) J_3, where the blue, green, and yellow lines are paths for J_1, J_2, and J_3, respectively.

the system. The corresponding variations of the magnetic anisotropic terms, such as D and J^{ani}, are also demonstrated in Fig. 8(a). For all the interactions, J_3-type interactions are found to be dominant over the other two types. For the present case, apart from the dominant J^{iso} interactions, the DMI parameters D also exhibit significant strength, which is generally expected for an NCS system. The existence of these various competing interactions in MGTO can essentially give rise to the observed noncollinear complex spin ordering.

F. Dielectric and magnetodielectric properties

The NCS spin-frustrated lattice in conjunction with an interesting complex noncollinear and noncoplanar helical-cycloidal spin ordering of MGTO (as per our NPD data analysis) renders the present system a potential source for hosting spin-driven MD and/or ME effect. Thus, this implies that the effect of the magnetic ordering on ε' of MGTO is worth investigating. Therefore, we investigated the T dependence of ε' of MGTO under various frequencies (f), with emphasis on the region near T_N, as illustrated in Fig. 9(a). A downturn behavior of ε' (T) curves in the vicinity of $T_N \sim 9$ K was observed, which led to a pronounced dielectric anomaly in the form of a dip, as shown in Fig. 9(a). The observed dielectric anomaly at T_N is interesting, as it essentially implies the close correspondence between the magnetic and dipolar properties of MGTO. Furthermore, the observed dielectric loss (tan δ) across the entire T range of our investigation remained extremely low (<0.01). This suggests the highly insulating character of MGTO, thus unequivocally eliminating the possibility of spurious experimental effects or extrinsic charge carriers affecting the ε' (T) curves. Moreover, the positions of the observed anomaly in the ε' (T) curves remained unchanged for different values of f. All the above-mentioned features of the ε' (T) curves suggest the occurrence of an intrinsic MD coupling as well as preclude any relaxation phenomenon in the system. If MD coupling does not occur in a system, then the ε' (T) curves generally obey the Barrett function, which is expressed as: $\varepsilon'(T) = \varepsilon'(0) + A/[\exp(\frac{\hbar\omega_0}{k_B T})-1]$, where A refers to the coupling constant and ω_0 denotes the average frequency for phonon modes presenting at lower wave numbers [41]. The ε' (T) data were consistent with the Barrett function at $T > T_N$, as shown in Fig. 9(b) [data only shown for $f = 1.5$ MHz under $H = 0$ T]. By contrast, the ε' (T) curve began deviating from Barrett's curve as T approached T_N, which indicates an underlying MD effect in the system. The best fitting yielded $\varepsilon'(0) = 19.65 \pm 1.01$, $A = 0.110 \pm 0.002$, and $\omega_0 = 85.5 \pm 0.6\,\mathrm{cm}^{-1}$. A similar scenario has been previously reported for various systems exhibiting MD effects.

To further validate the MD coupling, the ε' (T) curves were recorded under varying H values, as shown in Fig. 9(c). Interestingly, the ε' (T) curves were considerably suppressed as H increased, thus demonstrating strong coupling between the spin and dipolar degrees. Moreover, the line shapes of the ε' (T) curves altered significantly under H values exceeding H_c. This can be presumably attributed to field-induced spin-flip transition as observed in the M (H) curves, which consequently affect the dielectric properties via strong MD coupling. To further authenticate this assumption, we obtained the isothermal H variation of the ε' curve at $T = 2$ K (below

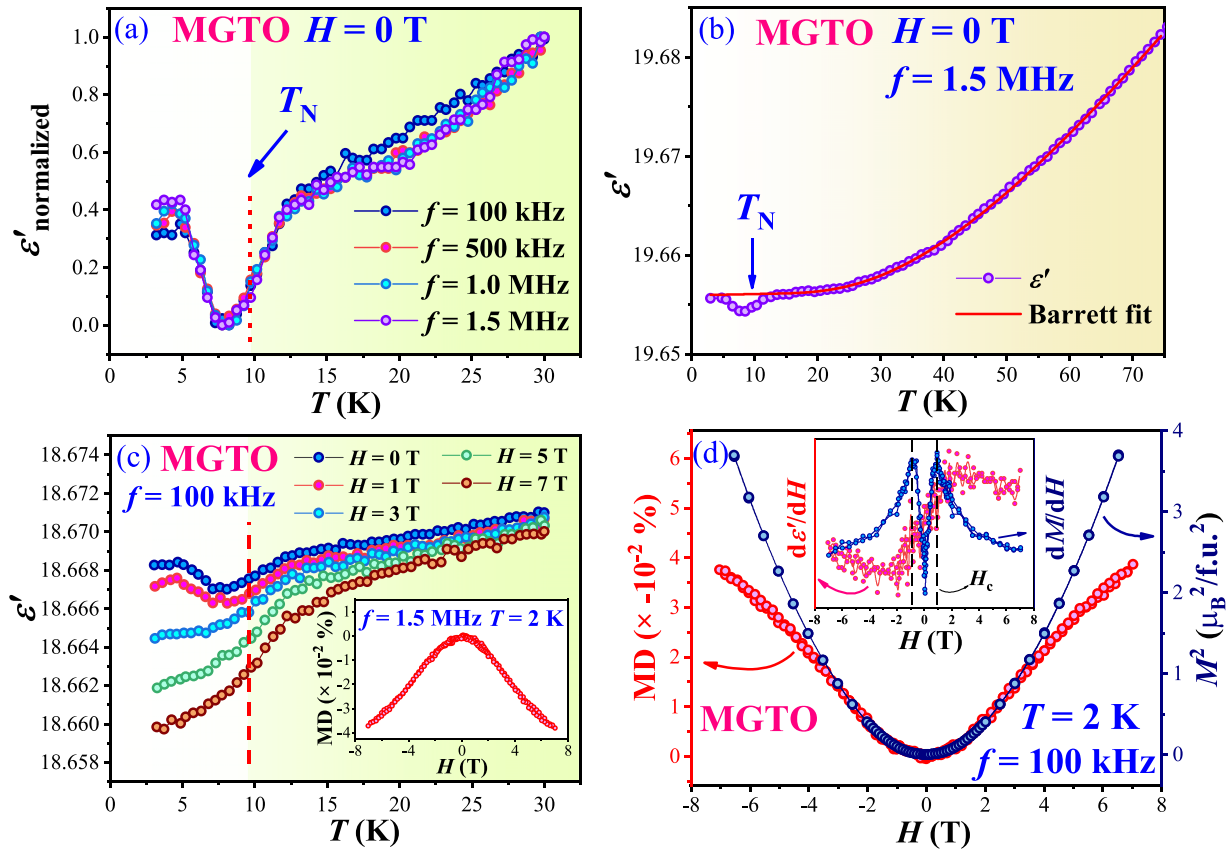

FIG. 9. (a) $\varepsilon'_{\text{normalized}}$ vs T curves at different f under zero field. Here, $\varepsilon'_{\text{normalized}} = (\varepsilon' - \varepsilon'_{\text{min}})/(\varepsilon'_{30\,\text{K}} - \varepsilon'_{\text{min}})$. (b) Thermal variation of ε' recorded at 1.5 MHz under $H = 0$ T and its best fit using the Barrett equation (shown in red) (c) ε' vs T curves at $f = 100$ kHz and under various H. Inset: Isothermal magnetic field variation of magnetodielectric coupling parameter MD (%) at $T = 2$ K. (d) H dependence of MD (%) and M^2 curves, which were recorded at $T = 2$ K. Inset: A comparison of dM/dH and $d\varepsilon'/dH$ curves as a function of H, which exhibit anomalies near the same critical field H_c.

T_N). The corresponding value of MD response (MD%) as a function of H was obtained using this expression: $\text{MD\%} = [\varepsilon'(0) - \varepsilon'(H)/\varepsilon'(0)] \times 100\%$, which is shown in the inset of Fig. 9(c). A noticeable alteration in slope occurs in the MD% vs H curve near H_c, indicating its cross coupling with the field-induced metamagnetic transition. This is particularly evident when examining the inset of Fig. 9(d), which illustrates the variations in H of dM/dH and $d\varepsilon'/dH$. For materials that demonstrate higher-order ME coupling, which is typically mediated by subtle lattice distortions, the behavior of MD% tends to be consistent with that of M^2. This type of MD behavior can be explained via the phenomenological Ginzburg-Landau theory. This theory establishes a correlation between the MD effect at lower H and an ME coupling term $\gamma P^2 M^2$ within the thermodynamic potential, using this expression [42]: $\Phi = \Phi_0 + \alpha P^2 - PE + \alpha' M^2 - MH + \gamma P^2 M$, where α, α', and γ represent the T-dependent MD coupling coefficients; P refers to the ferroelectric polarization; and E denotes the electric field. In this scenario, the linear M (H) curve at $T = 2$ K suggests a nonlinear dependence of the M^2 curve on H. Consequently, the MD% data closely followed the M^2 curve in the low-H regime, as depicted in Fig. 9(d). This appears to indicate the presence of weak ME coupling in MGTO. An isostructural distortion below T_N, spurred by the magnetostriction effect, has been observed in MGTO, which will be discussed in the following section. This distortion could be pivotal in instigating both the dielectric anomaly and the weak possible ME coupling in this system. Based on the inverse Dzyaloshinskii-Moriya (DM) model, the complex noncollinear spin structure may trigger a ferroelectric order [43]. Furthermore, Kaplan and Mahanti provided theoretical evidence for the development of ferroelectric polarization within a helical (proper screw) magnetic system [44,45]. They achieved this through an extended DM model, grounded in symmetry considerations. Their comprehensive theoretical investigation introduced an additional component $P \propto (S_i \times S_j)$, wherein S_i and S_j represent the two canted spins located at the ith and jth sites, respectively. This addition suggests that not only a cycloidal spiral spin ordering but also a helical spin structure may induce local polarization in a system. Therefore, a higher-order weak ME coupling in MGTO may also serve as an underlying origin for the observed MD effect in this system. However, our pyrocurrent (I_P) measurements could not trace a sizable signal for ferroelectric polarization below T_N. The lack of I_P signal may be attributed to the polycrystalline nature of the sample, which typically results in a significant suppression of the I_P signal, as reported earlier [46]. Nevertheless, additional experimental single-crystal studies and

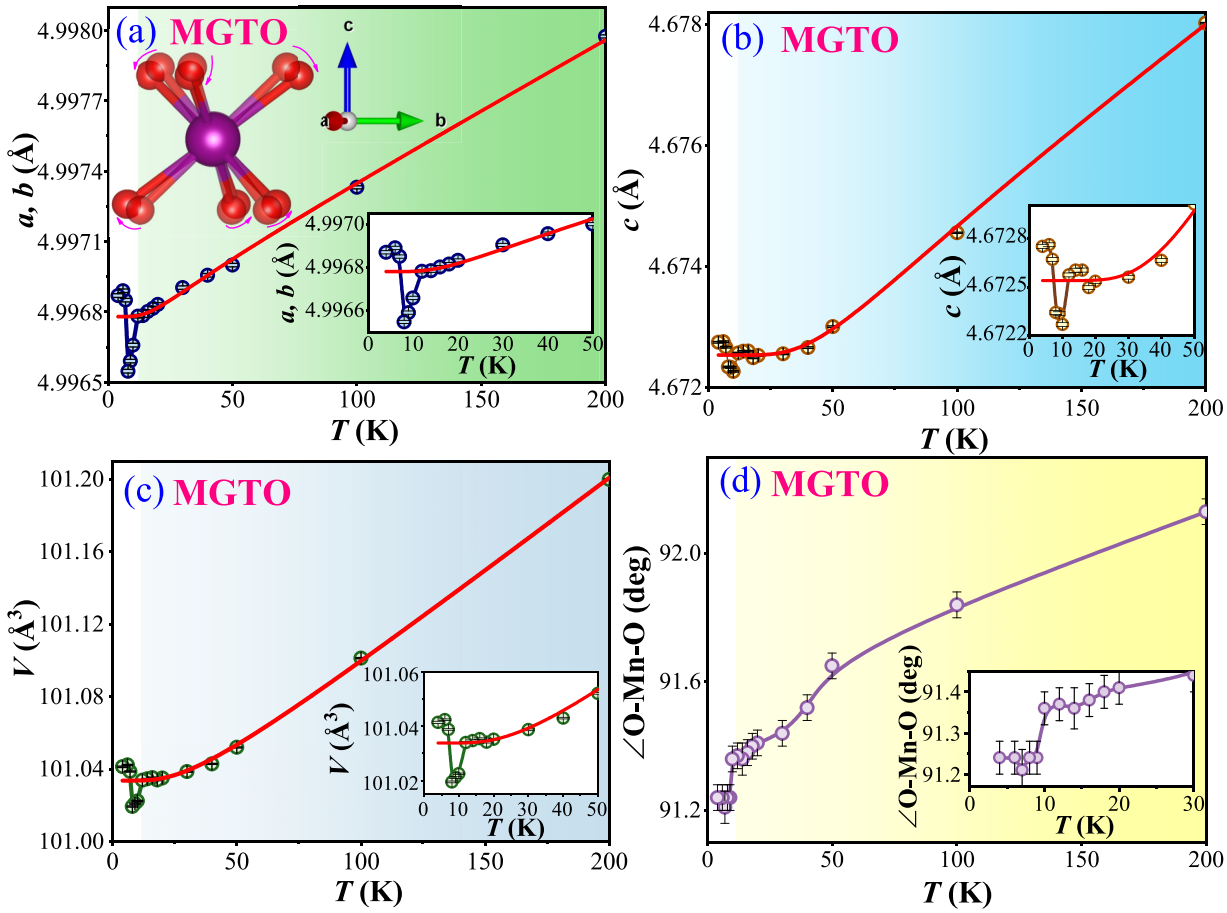

FIG. 10. The T variations of lattice parameters a, c, and V are demonstrated in (a)–(c), respectively. Insets (bottom) show a closer view of the respective curves near T_N. (d) depicts the thermal variation of the bond angle O–Mn–O related to MnO_6 octahedra. The inset shows its closer view near T_N. Inset of (a): A schematic representation of the distorted octahedra MnO_6, wherein lighter and deeper red-colored spheres refer to oxygen positions above and below T_N, respectively.

theoretical investigations are necessary to establish a definitive confirmation.

G. Magnetoelastic coupling: Temperature-dependent synchrotron XRD study

To probe the thermal evolution of the crystal structure of MGTO, particularly near its T_N, the T-dependent SXRD patterns were collected down to 4 K (as shown in Fig. S1 of SM [33]). Throughout the studied temperature range, no sizable changes in the patterns, such as peak splitting or the appearance of additional Bragg peaks, were observed. This essentially discards the occurrence of a global structural-phase transition. Further analysis using Rietveld refinement confirmed that all the collected SXRD patterns could be satisfactorily fitted with the trigonal crystal symmetry $P312$. The SXRD data recorded at $T = 200$ and 4 K along with their best fit are shown in Fig. S2 and the obtained crystallographic information is detailed in Table SI in SM [33]. The temperature variations of the obtained lattice parameters, such as a, c, and V, are demonstrated in Figs. 10(a)–10(c), respectively. Notably, all parameters displayed distinct anomalies near T_N, thus indicating an isostructural distortion through the magnetoelastic coupling. Consequently, the MnO_6 octahedra gets distorted below T_N [as pictorially demonstrated in the inset of Fig. 10(a)], which is manifested by a distinct anomaly observed in the O–Mn–O bond angle [as depicted in Fig. 10(d) and its inset]. Nevertheless, the magnetoelastic coupling can be validated by examining "the thermal expansion of various lattice parameters," which specifically entails elastic degrees of freedom. Assuming there is no structural change via magnetoelastic coupling, the temperature variations of various lattice parameters in a magnetic system, following thermal expansion behavior, can be described as: $a(T) = a_0[1 + \frac{Be^{d/T}}{T(e^{(d/T)}-1)^2}]$; $c(T) = c_0[1 + \frac{fe^{g/T}}{T(e^{(g/T)}-1)^2}]$; and $V(T) = V_0[1 + \frac{A}{(e^{\theta_D/T-1})}]$ [47]. In the equation, a_0, c_0, and V_0 denote the lattice constants at $T = 0$ K, while B, d, f, g, and A serve as the adjustable fitting parameters. θ_D represents the Debye temperature. Above T_N, the refined lattice parameters as a function of T are well described by the thermal expansion law. The obtained parameters from the best fitting are summarized in Table SIII of SM [33]. However, the lattice parameters showed large deviations from the thermal expansion law in the vicinity of T_N, thus suggesting an altered trend of the structural variation in the magnetically ordered region. This observation confirms the presence of magnetoelastic coupling, which evidently plays a

crucial role in the manifestation of the observed MD coupling in this system.

IV. CONCLUSION

Extensive experimental investigations were conducted on a chiral spin-frustrated TLAF system MGTO to unravel the intricate interplay between its complex spin ordering, lattice, and dielectric properties. (i) Below $T_N = 9$ K, a long-range ordered AFM state was observed through bulk magnetization, specific heat, and neutron powder-diffraction studies. (ii) Analysis of NPD data at $H = 0$ T revealed an incommensurate complex spin structure, which is best described as a mixture of a helical (major) and cycloidal (minor) spin arrangement characterized by a propagation vector $\boldsymbol{k} = (1/3, 1/3, 0.184)$, which got transformed into a conical spin ordering under application of magnetic field. (iii) DFT calculations also supported this complex spin structure (at $H = 0$ T) as an energetically favorable ground state. Exchange-interaction energy calculations indicated the presence of various competing AFM and FM interactions, which essentially trigger the noncollinear complex incommensurate spin ordering in this TLAF system. (iv) A pronounced dielectric anomaly emerged at T_N, which demonstrated substantial MD coupling. The H variations of ε' and M clearly reflected the $\varepsilon' \propto M^2$ relationship, thus indicating an underlying higher-order weak ME coupling. (v) Analysis of SXRD data yielded a sizable isostructural distortion due to magnetoelastic coupling below T_N, which appears to be a plausible origin for the observed pronounced MD and weak possible ME coupling.

ACKNOWLEDGMENTS

This study was supported by the National Science and Technology Council, Taiwan, under Grants No. MOST 110–2112-M-110–008-MY3, No. NSTC 111–2112-M-110–019, No. NSTC 111–2811-M-110–010, No. NSTC 112–2811-M-110–029, No. NSTC 112–2923-M-110–001, and No. NSTC 112–2112-M-110–018. We thank the ESRF for making their facilities available for Experiment No. IH-HC-4009 (doi.org/10.15151/ESRF-ES-1576260248). A.P. would like to thank SERB, India, for the NPDF funding (Grant No. PDF/2022/001020) and he is also thankful to the European Commission for their support granted through the Horizon Europe Marie Sklodowska-Curie Actions Individual Fellowship, with Project No. 101110742 — HiTempMagMat — HORIZON-MSCA-2022-PF-01.

[1] L. Balents, Spin liquids in frustrated magnets, Nature (London) **464**, 199 (2010).

[2] M. F. Collins and O. A. Petrenko, *Review/Synthèse:* Triangular antiferromagnets, Can. J. Phys. **75**, 605 (1997).

[3] A. P. Ramirez, Strongly geometrically frustrated magnets, Annu. Rev. Mater. Sci. **24**, 453 (1994).

[4] P. W. Anderson, Resonating valence bonds: A new kind of insulator?, Mater. Res. Bull. **8**, 153 (1973).

[5] S. Toth, B. Lake, S. A. J. Kimber, O. Pieper, M. Reehuis, A. T. M. N. Islam, O. Zaharko, C. Ritter, A. H. Hill, H. Ryll, K. Kiefer, D. N. Argyriou, and A. J. Williams, 120° helical magnetic order in the distorted triangular antiferromagnet α-$CaCr_2O_4$, Phys. Rev. B **84**, 054452 (2011).

[6] K.-Y. Choi, I. H. Choi, P. Lemmens, J. van Tol, and H. Berger, Magnetic, structural, and electronic properties of the multiferroic compound $FeTe_2O_5Br$ with geometrical frustration, J. Phys.: Condens. Matter **26**, 086001 (2014).

[7] S. Chattopadhyay, S. Petit, E. Ressouche, S. Raymond, V. Balédent, G. Yahia, W. Peng, J. Robert, M.-B. Lepetit, M. Greenblatt, and P. Foury-Leylekian, 3*d*-4*f* coupling and multiferroicity in frustrated Cairo Pentagonal oxide $DyMn_2O_5$, Sci. Rep. **7**, 14506 (2017).

[8] M. Lee, E. S. Choi, J. Ma, R. Sinclair, C. R. Dela Cruz, and H. D. Zhou, Magnetism and multiferroicity of an isosceles triangular lattice antiferromagnet $Sr_3NiNb_2O_9$, J. Phys.: Condens. Matter **28**, 476004 (2016).

[9] M. Lee, J. Hwang, E. S. Choi, J. Ma, C. R. Dela Cruz, M. Zhu, X. Ke, Z. L. Dun, and H. D. Zhou, Series of phase transitions and multiferroicity in the quasi-two-dimensional spin-1/2 triangular-lattice antiferromagnet $Ba_3CoNb_2O_9$, Phys. Rev. B **89**, 104420 (2014).

[10] M. Lee, E. S. Choi, X. Huang, J. Ma, C. R. Dela Cruz, M. Matsuda, W. Tian, Z. L. Dun, S. Dong, and H. D. Zhou, Magnetic phase diagram and multiferroicity of $Ba_3MnNb_2O_9$: A spin-5/2 triangular lattice antiferromagnet with weak easy-axis anisotropy, Phys. Rev. B **90**, 224402 (2014).

[11] J. Hwang, E. S. Choi, F. Ye, C. R. Dela Cruz, Y. Xin, H. D. Zhou, and P. Schlottmann, Successive magnetic phase transitions and multiferroicity in the spin-one triangular-lattice antiferromagnet $Ba_3NiNb_2O_9$, Phys. Rev. Lett. **109**, 257205 (2012).

[12] J. S. White, Ch. Niedermayer, G. Gasparovic, C. Broholm, J. M. S. Park, A. Y. Shapiro, L. A. Demianets, and M. Kenzelmann, Multiferroicity in the generic easy-plane triangular lattice antiferromagnet $RbFe(MoO_4)_2$, Phys. Rev. B **88**, 060409(R) (2013).

[13] V. Kocsis, Y. Tokunaga, T. Rõõm, U. Nagel, J. Fujioka, Y. Taguchi, Y. Tokura, and S. Bordács, Spin-lattice and magnetoelectric couplings enhanced by orbital degrees of freedom in polar multiferroic semiconductors, Phys. Rev. Lett. **130**, 036801 (2023).

[14] P. Park, K. Park, J. Oh, K. H. Lee, J. C. Leiner, H. Sim, T. Kim, J. Jeong, K. C. Rule, K. Kamazawa, K. Iida, T. G. Perring, H. Woo, S. W. Cheong, M. E. Zhitomirsky, A. L. Chernyshev, and J.-G. Park, Spin texture induced by non-magnetic doping and spin dynamics in 2D triangular lattice antiferromagnet *h*-$Y(Mn,Al)O_3$, Nat. Commun. **12**, 2306 (2021).

[15] W. Eerenstein, N. D. Mathur, and J. F. Scott, Multiferroic and magnetoelectric materials, Nature (London) **442**, 759 (2006).

[16] A. Pal, T. W. Kuo, C.-H. Hsu, D. Chandrasekhar Kakarla, A. Tiwari, M. C. Chou, A. Patra, P. Yanda, E. Blundo, A. Polimeni, A. Sundaresan, F. C. Chuang, and H. D. Yang, Interplay of

lattice, spin, and dipolar properties in $CoTeMoO_6$: Emergence of Griffiths-like phase, metamagnetic transition, and magnetodielectric effect, Phys. Rev. B **105**, 024420 (2022).

[17] S.-W. Cheong and M. Mostovoy, Multiferroics: A magnetic twist for ferroelectricity, Nat. Mater. **6**, 13 (2007).

[18] B. Poojitha, A. Rathore, A. Kumar, and S. Saha, Signatures of magnetostriction and spin-phonon coupling in magnetoelectric hexagonal 15*R*-$BaMnO_3$, Phys. Rev. B **102**, 134436 (2020).

[19] A. Pal, C. H. Huang, T. W. Yen, P. H. Lee, Y. H. Chang, C. H. Yeh, T. W. Kuo, A. Tiwari, D. Chandrasekhar Kakarla, S. M. Huang, M. C. Chou, H. S. Kunwar, S. Rana, V. G. Sathe, B. H. Chen, Y. C. Chuang, and H. D. Yang, Spin-induced strongly correlated magnetodielectricity, magnetostriction effect, and spin-phonon coupling in helical magnet $Fe_3(PO_4)O_3$, Phys. Rev. B **106**, 094404 (2022).

[20] M. A. Prosnikov, A. N. Smirnov, V. Yu. Davydov, Y. Araki, T. Arima, and R. V. Pisarev, Lattice and magnetic dynamics in the polar, chiral, and incommensurate antiferromagnet Ni_2InSbO_6, Phys. Rev. B **100**, 144417 (2019).

[21] J. W. Kim, S. Khim, S. H. Chun, Y. Jo, L. Balicas, H. T. Yi, S.-W. Cheong, N. Harrison, C. D. Batista, J. Hoon Han, and K. H. Kim, Manifestation of magnetic quantum fluctuations in the dielectric properties of a multiferroic, Nat. Commun. **5**, 4419 (2014).

[22] K. Kimura, P. Babkevich, M. Sera, M. Toyoda, K. Yamauchi, G. S. Tucker, J. Martius, T. Fennell, P. Manuel, D. D. Khalyavin, R. D. Johnson, T. Nakano, Y. Nozue, H. M. Rønnow, and T. Kimura, Magnetodielectric detection of magnetic quadrupole order in $Ba(TiO)Cu_4(PO_4)_4$ with Cu_4O_{12} square cupolas, Nat. Commun. **7**, 13039 (2016).

[23] C.-W. Nan and J.-M. Liu, Multiferroics: A beautiful but challenging multi-polar world, Natl. Sci. Rev. **6**, 620 (2019).

[24] H. C. Wu, K. Devi Chandrasekhar, J. K. Yuan, J. R. Huang, J.-Y. Lin, H. Berger, and H. D. Yang, Anisotropic spin-flip-induced multiferroic behavior in kagome $Cu_3Bi(SeO_3)_2O_2Cl$, Phys. Rev. B **95**, 125121 (2017).

[25] T. Aoyama, Y. Hasegawa, S. Kimura, T. Kimura, and K. Ohgushi, Anisotropic magnetodielectric effect in the honeycomb-type magnet α-$RuCl_3$, Phys. Rev. B **95**, 245104 (2017).

[26] A. Tiwari, D. Chandrasekhar Kakarla, M. J. Hsieh, J. Y. Lin, C. W. Wang, L. K. Tseng, C. E. Lu, A. Pal, T. W. Kuo, M. M. C. Chou, and H. D. Yang, Observation of magnetic field-induced second magnetic ordering and peculiar ferroelectric polarization in L-type ferrimagnetic $Fe_2(MoO_4)_3$, Phys. Rev. Mater. **6**, 094412 (2022).

[27] G. Lawes, A. P. Ramirez, C. M. Varma, and M. A. Subramanian, Magnetodielectric effects from spin fluctuations in isostructural ferromagnetic and antiferromagnetic systems, Phys. Rev. Lett. **91**, 257208 (2003).

[28] K. Devi Chandrasekhar, J. Krishna Murthy, J.-Y. Lin, H. C. Wu, W. J. Tseng, A. Venimadhav, and H. D. Yang, Magnetostructural coupling and multiferroic properties in the spin-frustrated system $Ni_{1-x}Zn_xCr_2O_4$, Phys. Rev. B **94**, 205143 (2016).

[29] C. H. Prashanth, T. W. Yen, A. Tiwari, P. Athira, S. M. Huang, B. Poojitha, D. P. Gulo, H. L. Liu, C. W. Wang, Y. K. Lin, Y. C. Chuang, Y. C. Lai, K. Jyothinagaram, H. D. Yang, and D. C. Kakarla, Interplay of magnetic and electric coupling across the spin density wave to conical magnetic ordering in a $BaHoFeO_4$ spin-cluster chain compound, J. Alloys Compd. **942**, 169017 (2023).

[30] S. W. Kim, Z. Deng, S. Yu, H. Padmanabhan, W. Zhang, V. Gopalan, C. Jin, and M. Greenblatt, A(II)$GeTeO_6$ (A = Mn, Cd, Pb): Non-centrosymmetric layered tellurates with $PbSb_2O_6$-related structure, Inorg. Chem. **56**, 9019 (2017).

[31] A. J. Studer, M. E. Hagen, and T. J. Noakes, Wombat: The high-intensity powder diffractometer at the OPAL reactor, Phys. B: Condens. Matter **385–386**, 1013 (2006).

[32] M. Avdeev and J. R. Hester, ECHIDNA: A decade of high-resolution neutron powder diffraction at OPAL, J. Appl. Crystallogr. **51**, 1597 (2018).

[33] See Supplemental Material at http://link.aps.org/supplemental/10.1103/PhysRevB.110.064405 for the details of the theoretical calculation approach, lattice information, temperature variation of the XRD pattern, and additional data of $MnGeTeO_6$.

[34] P. T.-W. Yen, H.-C. Wu, and S.-M. Huang, First-principles study of the crystal and magnetic structures of multiferroic Cu_2OCl_2, J. Phys. Condens. Matter **34**, 335602 (2022).

[35] G. D. Dwivedi, T.-W. Yen, S. M. Kumawat, C. W. Wang, D. C. Kakarla, A. Tiwari, H. D. Yang, S. M. Huang, C. M. Chung, S. J. Sun, and H. Chou, Switching of dominant magnetic exchange interactions between tetrahedral–octahedral and octahedral–octahedral sites in $(Mn_{1-x}Cr_x)_3O_4$ spinels, J. Mater. Chem. C **11**, 11312 (2023).

[36] X. He, N. Helbig, M. J. Verstraete, and E. Bousquet, TB2J: A python package for computing magnetic interaction parameters, Comput. Phys. Commun. **264**, 107938 (2021).

[37] J. Khatua, T. Arh, B. S., S. B. Mishra, H. Luetkens, A. Zorko, B. Sana, M. S. Ramachandra Rao, B. R. K. Nanda, and P. Khuntia, Development of short and long-range magnetic order in the double perovskite based frustrated triangular lattice antiferromagnet Ba_2MnTeO_6, Sci. Rep. **11**, 6959 (2021).

[38] P. Saeaun, Y. Zhao, P. Piyawongwatthana, T. J. Sato, F. C. Chou, M. Avdeev, G. Gitgeatpong, and K. Matan, Magnetic properties and magnetic structure of the frustrated quasi-one-dimensional antiferromagnet $SrCuTe_2O_6$, Phys. Rev. B **102**, 134407 (2020).

[39] L. D. Sanjeewa, V. O. Garlea, M. A. McGuire, C. D. McMillen, and J. W. Kolis, Magnetic ground state crossover in a series of glaserite systems with triangular magnetic lattices, Inorg. Chem. **58**, 2813 (2019).

[40] J. M. Hastings and L. M. Corliss, Magnetic structure of manganese chromite, Phys. Rev. **126**, 556 (1962).

[41] P. T. Barton, M. C. Kemei, M. W. Gaultois, S. L. Moffitt, L. E. Darago, R. Seshadri, M. R. Suchomel, and B. C. Melot, Structural distortion below the Néel temperature in spinel $GeCo_2O_4$, Phys. Rev. B **90**, 064105 (2014).

[42] A. Indra, K. Dey, J. K. Dey, S. Majumdar, U. Rütt, O. Gutowski, M. v. Zimmermann, and S. Giri, CrO_4 distortion-driven ferroelectric order in (R, Y) CrO_4 (R = Sm, Gd, and Ho): A new family of multiferroics, Phys. Rev. B **98**, 014408 (2018).

[43] H. Katsura, N. Nagaosa, and A. V. Balatsky, Spin current and magnetoelectric effect in noncollinear magnets, Phys. Rev. Lett. **95**, 057205 (2005).

[44] T. A. Kaplan and S. D. Mahanti, Canted-spin-caused electric dipoles: A local symmetry theory, Phys. Rev. B **83**, 174432 (2011).

[45] A. Albaalbaky, Y. Kvashnin, D. Ledue, R. Patte, and R. Frésard, Magnetoelectric properties of multiferroic $CuCrO_2$ studied by

means of *ab initio* calculations and Monte Carlo simulations, Phys. Rev. B **96**, 064431 (2017).

[46] L. Zhao, C.-H. Du, and A. C. Komarek, Spin-driven pyroelectricity in Ni_3TeO_6 without ferroelectric signatures of the transition at Néel temperature, Phys. Status Solidi RRL **11**, 1700073 (2017).

[47] A. Pal, T. W. Yen, T. W. Kuo, C. W. Wang, S. M. Huang, M. C. Chou, Y. C. Lai, Y. C. Chuang, P. Yanda, A. Sundaresan, H. S. Kunwar, V. G. Sathe, A. Tiwari, D. C. Kakarla, and H. D. Yang, Unconventional multiferroicity induced by structural distortion and magnetostriction effect in the layered spin-1/2 ferrimagnet $Bi_2Cu_5B_4O_{14}$, Phys. Rev. B **107**, 184430 (2023).